



**HAL**  
open science

## Structural and electrical properties of large area epitaxial VO<sub>2</sub> films grown by electron beam evaporation

Virginie Théry, Alexandre Boulle, Aurelian Crunteanu, Jean-Christophe Orlianges, Arnaud Beaumont, Richard Mayet, Amine Mennai, Françoise Cosset, Annie Bessaudou, Fabert Marc

### ► To cite this version:

Virginie Théry, Alexandre Boulle, Aurelian Crunteanu, Jean-Christophe Orlianges, Arnaud Beaumont, et al.. Structural and electrical properties of large area epitaxial VO<sub>2</sub> films grown by electron beam evaporation. *Journal of Applied Physics*, 2017, 121 (5), pp.055303. 10.1063/1.4975117. hal-01455047

**HAL Id: hal-01455047**

**<https://unilim.hal.science/hal-01455047>**

Submitted on 3 Feb 2017

**HAL** is a multi-disciplinary open access archive for the deposit and dissemination of scientific research documents, whether they are published or not. The documents may come from teaching and research institutions in France or abroad, or from public or private research centers.

L'archive ouverte pluridisciplinaire **HAL**, est destinée au dépôt et à la diffusion de documents scientifiques de niveau recherche, publiés ou non, émanant des établissements d'enseignement et de recherche français ou étrangers, des laboratoires publics ou privés.

# Structural and electrical properties of large area epitaxial VO<sub>2</sub> films grown by electron beam evaporation

V. Théry,<sup>1</sup> A. Boule,<sup>1</sup> A. Crunteanu,<sup>2</sup> J. C. Orlianges,<sup>2</sup> A. Beaumont,<sup>2</sup> R. Mayet,<sup>1</sup> A. Mennai,<sup>2</sup> F. Cosset,<sup>2</sup> A. Bessaudou,<sup>2</sup> and M. Fabert<sup>2</sup>

<sup>1</sup>*Sciences des Procédés Céramiques et Traitements de Surfaces, CNRS UMR 7315, Centre Européen de la céramique, 12 rue Atlantis, 87068 Limoges Cedex, France*

<sup>2</sup>*XLIM, UMR 7252 CNRS/ University of Limoges, 123 Av. Albert Thomas, 87060 Limoges, France.*

(Dated: 16 January 2017)

Large area (up to 4 squared inches) epitaxial VO<sub>2</sub> films, with a uniform thickness and exhibiting an abrupt metal-insulator transition with a resistivity ratio as high as  $2.85 \times 10^4$  have been grown on (001)-oriented sapphire substrates by electron beam evaporation. The lattice distortions (mosaicity) and the level of strain in the films have been assessed by X-ray diffraction. It is demonstrated that the films grow in a domain-matching mode where distortions are confined close to the interface which allows to grow high-quality materials despite the high film-substrate lattice mismatch. It is further shown that a post-deposition high-temperature oxygen annealing step is crucial to ensure the correct film stoichiometry and provide the best structural and electrical properties. Alternatively, it is possible to obtain high quality films with an RF discharge during deposition, which hence do not require the additional annealing step. Such films exhibit similar electrical properties and only slightly degraded structural properties.

## I. INTRODUCTION

Vanadium dioxide (VO<sub>2</sub>) is an important strongly electron correlated material undergoing a first-order temperature-induced transition between a room-temperature insulator and a conductive, metallic state, for temperatures higher than a transition temperature,  $T_{MIT}$ , situated around 68°C (341 K)<sup>1,2</sup>. The electronic metal-insulator transition (MIT) in VO<sub>2</sub> occurs concomitantly with a structural phase transition in which the material evolves from a monoclinic M phase (at temperatures below  $T_{MIT}$ ) to a rutile R phase for temperatures higher than  $T_{MIT}$ <sup>1,2</sup>. The phase transition in VO<sub>2</sub> thin films and nanostructures can be triggered thermally but also optically<sup>3</sup>, or by electric fields or current injection<sup>4-6</sup>, resulting in drastic changes in the material's electrical, optical and structural properties. The abrupt, extreme resistivity change over the MIT in VO<sub>2</sub> thin films, which can reach up to five orders of magnitude, along with the onset of unusual nonlinear electrical and optical properties (e.g. negative differential resistance<sup>7</sup> or negative differential emissivity in the far-infrared domain<sup>8</sup>) makes the material highly desirable for electronic and photonic applications such as Mott-FET devices<sup>4</sup>, nano-oscillators<sup>7</sup>, optical switches or coatings with modulated transmission<sup>8</sup> etc. The development of reliable deposition methods for obtaining VO<sub>2</sub> thin films with reproducible properties over large substrates surfaces is thus crucial for future developments of the material and its large-scale introduction in practical applications but also, from a fundamental point of view, to assess the current VO<sub>2</sub> phase transition models relevant to the physics of strongly correlated materials.

Various deposition techniques have been used to grow VO<sub>2</sub> thin films showing the expected metal-insulator transition. Among the most employed ones are PVD-

based methods like pulsed laser deposition<sup>9</sup> and DC or RF magnetron sputtering<sup>9-11</sup> but CVD or sol-gel methods can be also exploited for obtaining VO<sub>2</sub> films, doped VO<sub>2</sub> composites and nanoparticles<sup>9,12</sup>. One of the major drawbacks of the physical deposition methods are the costs associated with the target materials and the high-vacuum deposition systems as well as the lack of film uniformity over large-area substrates usually employed in micro-electronics and optical fabrication technologies. On the other hand, the CVD and sol-gel processes involve complex chemistry which is often incompatible with specific substrates or technological development of VO<sub>2</sub>-based devices. Large area (wafer-scale) films of VO<sub>2</sub> could successfully be grown on sapphire substrates, with diameters up to 3 inches, using molecular beam epitaxy<sup>13,14</sup> although the cost and the complexity of this technique remains an issue. Compared to the above-mentioned deposition methods, the electron-beam evaporation is rather an affordable technique which can be successfully employed to obtain crystalline high-quality, uniform VO<sub>2</sub> layers on different types of substrates (sapphire, SiO<sub>2</sub> /Si, Si...)<sup>5,8,15-18</sup>.

In this work, we investigated the structural and electronic properties of epitaxial VO<sub>2</sub> films grown on sapphire substrates as large as four squared inches. It is now well understood that the electrical properties of VO<sub>2</sub> materials are tightly bound with the level of strain<sup>19-26</sup> and the oxygen content in the material<sup>27-30</sup>. Special attention has therefore been paid to these aspects, using in-depth X-ray diffraction (XRD) measurements combined with numerical simulations which allowed us to rationalize the evolution of the final properties of VO<sub>2</sub> films for varying deposition conditions. It is demonstrated that large area VO<sub>2</sub> films, with a uniform thickness and exhibiting an abrupt MIT with a resistivity ratio as high as  $2.85 \times 10^4$  can be grown, provided that the oxygen content is close the stoichiometric composition.

## II. EXPERIMENTAL DETAILS

## A. Film growth

The  $\text{VO}_2$  films have been grown using an electron-beam evaporation system inside a high-vacuum chamber (evacuated to a base pressure of  $5 \times 10^{-5}$  Pa prior to the deposition) using the electron-beam evaporation of a metallic vanadium target under oxygen atmosphere. The vanadium target is placed in a crucible  $\sim 200$  mm below the substrate holder and is evaporated by an incident electron beam (accelerating voltage of 10 kV) under pure oxygen atmosphere (working pressure  $\sim 8 \times 10^{-2}$  Pa and oxygen flow of  $\sim 5.4$  sccm)<sup>5</sup>. Thin films with a 100 nm nominal thickness were grown at deposition rates not exceeding  $0.05 \text{ nm}\cdot\text{s}^{-1}$  on (001)-oriented  $2 \times 2$  inches sapphire substrates heated at  $500^\circ\text{C}$ . The optimization of the growth process revealed that a subsequent in-situ annealing at  $550^\circ\text{C}$  under pure oxygen atmosphere (without V evaporation) was necessary to obtain films with the desired quality. In order to investigate the role of this post-growth treatment, a first series of samples has been grown without annealing. In the following, these films are referred to as “**as-grown**” films.

After complete structural and physical characterizations, these films were submitted to the post-deposition annealing process at  $550^\circ\text{C}$  under oxygen atmosphere (base pressure of 0.5 Pa) for 15 minutes. In the following, these films are referred to as “**annealed**” films. As will be shown below, the post-deposition annealing procedure is an essential step for obtaining high quality  $\text{VO}_2$  films. The obtained films are highly uniform, with homogeneous thicknesses even on sapphire wafers with edge length as large as two-inches, with root-mean squared roughness of 2.4 nm as recorded by atomic force microscopy. As an example, Figure 1 shows a  $\text{VO}_2$  “annealed” layer obtained on a two inches sapphire substrate, along with the thickness distribution over the entire surface deduced from ellipsometer mapping measurements. The obtained film, with a targeted thickness of 100 nm shows extremely uniform coverage, with a thickness variation comprised between 107-111 nm on most of the deposition area.

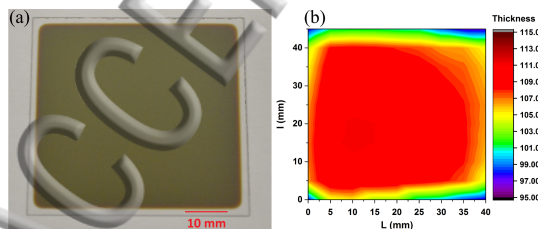


FIG. 1. (a) Optical photography of a 100-nm thick  $\text{VO}_2$  layer obtained on a large area sapphire substrate (two inches edge length) and (b) the associated thickness mapping as deduced from ellipsometric measurements

Alternatively, the growth procedure was modified by polarizing the sapphire substrates (during the entire deposition process) by using a RF generator with an in-

cident power fixed to 50 W. As indicated elsewhere<sup>5</sup>, the RF source, on one hand, is creating reactive species through the onset of an  $\text{O}_2$  plasma containing evaporated V atoms in the space between the vanadium crucible and the substrate and, on the other hand, it may enhance, at the substrate level, the adhesion and the compactness of the growing films. The films grown using this alternative process are referred to as “**discharge**” samples and are not subjected to post-deposition thermal annealing.

## B. Structural and electrical characterization

The electrical resistivity variation with temperature across the MIT of the obtained layers was recorded in the  $25 - 95^\circ\text{C}$  temperature interval and have been measured using the four-probes technique. We used a custom set-up employing four in-line spring-loaded probes (spaced by 1 mm) coupled to a Keithley 2612B sourcemeter. A Peltier element was used to control the heating/ cooling of the samples while the temperature was monitored by a Pt-100 thermocouple attached near the films’ surfaces.

Raman spectroscopy measurements have been carried out using a Raman inverted microscope (Horiba LabRAM HR Evolution) using a continuous HeNe laser light ( $\lambda = 632.8 \text{ nm}$ ) with an incident power of 6 mW and focused on the sample with a  $60 \times$  objective (Nikon S plan fluor ELWD, numerical aperture of 0.7) to a spot of  $\sim 2 \mu\text{m}$  in diameter. As above, a Peltier element was used to control the heating/cooling of the samples while the temperature was monitored by a Pt-100 thermocouple attached near the films’ surfaces. The large-area mapping of thickness was performed using a spectroscopic ellipsometer (Horiba Jobin Yvon, UVISSEL) in the energy range 0.6-6.5 eV at room temperature.

XRD experiments have been performed on a Bruker “D8 discover” diffractometer equipped with a parabolic multilayer mirror, a two-reflection asymmetrically cut  $\text{Ge}(220)$  monochromator ( $\text{Cu K}\alpha_1$  radiation,  $\lambda = 1.5406 \text{ \AA}$ ) as primary optics and linear position sensitive detector covering a  $2^\circ 2\theta$  range with a  $0.01^\circ$  angular resolution.  $\theta - 2\theta$  scans have been performed over a wide  $2\theta$  range ( $2\theta = 30 - 95^\circ$ ) to probe the out-of-plane orientation, whereas  $\phi$ -scans, using the (220) reflection of  $\text{VO}_2$  and the (104) reflection of sapphire, have been used to determine the in-plane orientation of the films. Additionally, high-resolution  $\theta - 2\theta$  scans and  $\omega$ -scans (scanning incidence angle  $\omega$  at fixed  $2\theta$ ) have been performed through the (020) and (040) reflections of  $\text{VO}_2$ . The former scans give access to structural information in the out-of-plane direction, such as film thickness, homogeneous and heterogeneous strains. The latter  $\omega$ -scans provide structural information in the direction parallel to the surface (in-plane direction), such as the mosaicity and the lateral crystallite size.

Figure 2 and 3 display the XRD data recorded for the three type of films. In the  $\theta - 2\theta$  scans displayed in Fig. 2(a) only  $(0k0)$  reflections from  $\text{VO}_2$  and  $(00l)$  reflections from sapphire are observed which demonstrates that, for all three type of samples with a thickness of 100-nm, the  $\text{VO}_2$  films grow with the  $(010)$  planes parallel to the  $(001)$  planes of sapphire. This orientation is commonly observed for the  $\text{VO}_2$  system<sup>25,27,31</sup>. The in-plane orientation, determined from the  $\phi$ -scans, Fig. 2(b), reveal a six-fold symmetry instead of the two-fold symmetry expected for the  $(220)$  planes. This discrepancy is well known and is due to the existence of three structurally equivalent orientations of the  $(010)$  planes with respect to the  $(001)$  plane of sapphire, hence giving rise to three in-plane epitaxial variants<sup>25,27,31</sup>. The corresponding epitaxial relationships read:  $[100]\text{VO}_2 \parallel [210]\text{Al}_2\text{O}_3$ ,  $[100]\text{VO}_2 \parallel [-110]\text{Al}_2\text{O}_3$  and  $[100]\text{VO}_2 \parallel [120]\text{Al}_2\text{O}_3$ . It can also be also be noticed that the  $(220)$  peaks from  $\text{VO}_2$  are broad and splitted (with satellite peaks appearing at approximately  $\pm 2.5^\circ$ , as indicated by the arrows). This is due to angle mismatch between the  $\beta$  angle of  $\text{VO}_2$  ( $122.6^\circ$ ) and the  $\gamma$  angle of  $\text{Al}_2\text{O}_3$  ( $120^\circ$ ), as already observed in this system<sup>27</sup>.

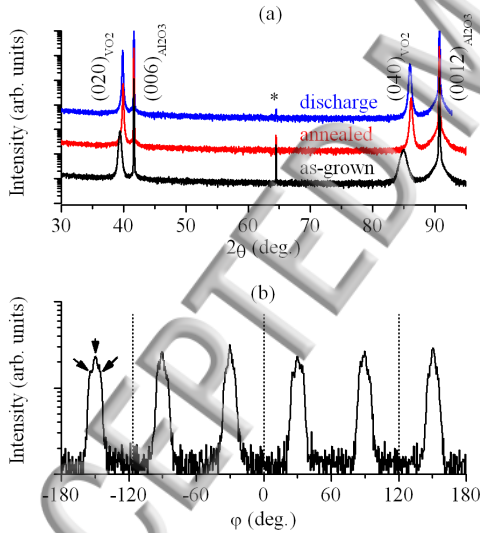


FIG. 2. (a)  $\theta - 2\theta$  scan of three different 100 nm thick films (black: as-grown; red: annealed; blue: discharge). The peak labeled “\*” correspond to the forbidden 009 reflection of sapphire which is excited by multiple diffraction. (b) typical  $\phi$ -scan recorded from the  $(220)$  planes of  $\text{VO}_2$ . The dotted lines indicate the positions of the  $(104)$  peaks of sapphire.

A closer inspection of Fig. 2(a) reveals that the  $(0k0)_{\text{VO}_2}$  peak in the as-grown sample is significantly shifted towards lower  $2\theta$  values as compared to the annealed and discharge films (which are relatively close to

Sample	$t(\text{nm})$	$D(\text{nm})$	$b$ (Å)	$\varepsilon_{zz}(\%)$	$\varepsilon_{xx}$ (°)	$\xi(\text{nm})$
as-grown	132		4.5644(3)	0.41	0.91	$+\infty$
			[0.84]			
annealed	107	$\sim 400$	4.5101(3)	0.11	0.68	9.5
			[-0.36]			
discharge	105	$\sim 300$	4.5180(3)	0.11	0.28	14
			[-0.18]			

TABLE I. Parameters (see text for definitions) obtained from the simulation of the  $\theta - 2\theta$  scans and  $\omega$ -scans for each type of film.

each other), which indicates a larger lattice parameter. The peak position provides, through Bragg’s law, the planar spacing  $d_{020}$ , and consequently the lattice parameter  $b = 2d_{020}$  of  $\text{VO}_2$ . The deviation of the observed lattice parameter from its theoretical value  $b^{\text{th}}$ , will be quantified using the out-of-plane strain:

$$e_{zz} = \frac{b - b^{\text{th}}}{b^{\text{th}}} \quad (1)$$

where  $b^{\text{th}} = 4.52596 \text{ \AA}^{32}$  and the subscript ‘zz’ indicates that this strain correspond to the third diagonal component of the strain tensor, the  $z$  axis being chosen normal the surface and the  $x$  axis is in the surface of the film in the direction of the X-ray beam. The strain might either be of mechanical origin, *i.e.* lattice and/or thermal expansion mismatch, or of chemical origin, *i.e.* deviations from the nominal V/O stoichiometry. In the growth mechanism proposed by Chen et al.<sup>25</sup>, the  $\text{V}^{4+}$  ions form bonds with the substrate surface  $\text{O}^{2-}$  ions and stack on a triangle of the  $\text{O}^{2-}$  ions to minimize the electrostatic potential. The interfacial strain hence originates from the distance misfit between  $\text{V}^{4+}$  ions in the  $\text{VO}_2$  structure and the centre of the  $\text{O}^{2-}$  triangles in the sapphire structure. This correspond to huge epitaxial strains of -4.4% (compressive) along  $[100]\text{VO}_2$  and 2.1% (tensile) along  $[001]\text{VO}_2$  which in general prohibits any possibility of pseudomorphic (lattice-matched) growth. In such cases the growth generally takes place by domain-matching epitaxy where different integral multiples of lattice planes match across the interface, *i.e.*  $n_f$  lattice planes of the film match  $n_s$  lattice planes of the substrate and  $n_f \neq n_s$  so as to relax the epitaxial strain. The region of bad matching gives rise to a so-called geometric dislocation<sup>33,34</sup>. In an earlier work it has been demonstrated that the  $\text{VO}_2$  films indeed grow in strain-relaxed state and elastic strain is stored in the film upon cooling down from the growth temperature as a result of the mismatch of the film and substrate thermal expansion coefficients<sup>35</sup>.

The strain values computed from Eq.(1) are reported in Table I. It is readily observed that the annealed and discharge films are compressively strained in the out-of-plane direction (-0.36% and -0.18%, respectively), in good agreement with the thermal expansion mismatch of the  $\text{VO}_2/\text{Al}_2\text{O}_3$  system<sup>35</sup> (note that the value -0.18%

observed for the discharge film is lower than the value expected for a 100 nm film; this point will be discussed in the following sections). On the contrary, the as-grown film exhibits an unexpected tensile strain (0.84%) in the out-of-plane direction, *i.e.* the lattice parameter is larger than the theoretical value, which can not be accounted for with the thermal expansion mismatch, nor with the lattice mismatch. This indicates that the as-grown films probably don't exhibit the correct stoichiometry.

In addition to the position shift, the  $(0k0)_{VO_2}$  peak in the as-grown film are also significantly broader than for the annealed and discharge films which might indicate a poorer crystalline quality. The intensity distribution of the XRD peaks is indeed sensitive to the micro- and nanostructure of the analysed films. In particular, considering the symmetrical  $(0k0)_{VO_2}$  reflections,  $\theta - 2\theta$  scans are sensitive to the film thickness, thickness fluctuation (*i.e.* roughness) and the  $zz$  components of the homogeneous and heterogeneous strain tensor, whereas  $\omega$ -scans are sensitive to the lateral extension of the crystallites and the  $xz$  component of the heterogeneous strain tensor (*i.e.* mosaicity)<sup>36</sup>. These points are addressed in the following sections, starting with the  $\theta - 2\theta$  scans.

## B. Out-of-plane nanostructure

For a symmetrical reflection with reciprocal lattice vector  $(0, h_z, 0)$ , the intensity distribution in the direction normal to the interface is given by<sup>36</sup>:

$$I(q_z) = \int dz.R(z)V(z)G(z)\exp(iq_z z) \quad (2)$$

where  $q_z$  is the deviation (in the  $z$  direction) of the scattering vector  $\mathbf{Q}$  ( $Q = 4\pi \sin\theta/\lambda$ ) from the Bragg position ( $q_z = Q_z - h_z$ ) and  $Q_z$  is the out-of-plane component of the scattering vector.  $V(z)$  is the correlation volume which depends on the average film thickness,  $\langle t \rangle$ , and the root-mean-squared (rms) roughness,  $\sigma_t$ <sup>36</sup>:

$$V(z) = \frac{1}{2} \operatorname{erfc} \left( \frac{z - \langle t \rangle}{\sqrt{2}\sigma_t} \right) + \frac{\sigma_t}{\sqrt{2\pi}} \exp \left[ -\frac{1}{2} \left( \frac{z - \langle t \rangle}{\sigma_t} \right)^2 \right] \quad (3)$$

In writing down the previous equation we implicitly assumed a normal (Gaussian) thickness distribution function, which is in general well suited to describe roughness in thin films, especially for films exhibiting a rather low roughness.  $G(z)$  is the correlation function of the crystal strain<sup>37</sup> that describes the effect of heterogeneous strain, *i.e.* random fluctuations of the strain,  $\delta e_{zz}$ , around its average value  $e_{zz}$  (analysed in the previous section). The exact expression of  $G(z)$  depends on the nature of the defects responsible for the heterogeneous strain. When these defects are *a priori* unknown, it is then useful to have recourse to a phenomenological description of the state of strain<sup>38</sup>. In such a description we assume  $\delta e_{zz}$  to obey some particular probability distribution function.

For instance, in the case of a centred symmetrical Lévy-stable distribution function, we obtain<sup>38</sup>:

$$G(z) = \exp \left( -\frac{1}{2} |h_z z|^\gamma \varepsilon_{zz}^\gamma \right) \quad (4)$$

where  $\gamma \in (0, 2]$  is the tail index of the distribution (for instance,  $\gamma = 2$  for a Gaussian distribution,  $\gamma = 1$  for a Lorentzian distribution). The Lévy-stable distribution, used in the present work, has proven to be better suited to describe the distribution of strain in materials<sup>38-42</sup> than the usual Gaussian distribution. In this case,  $\varepsilon_{zz}$  is the 'characteristic width' of the distribution of  $\delta e_{zz}$ <sup>38</sup>. Finally,  $R(z)$  is the Fourier transform of the resolution function of the diffractometer which is very well described by a Gaussian function whose width is estimated from the peak width of the sapphire peaks.

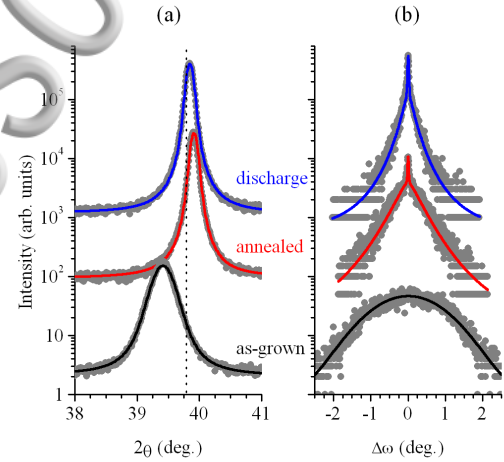


FIG. 3.  $\theta - 2\theta$  scans (a) and  $\omega$  scans (b) for each type of film. Grey dots: experimental data; line: simulation (black: as-grown; red: annealed; blue: discharge). The curves are shifted vertically for clarity.

Equations (2)-(4) have been used to simulate the experimental  $\theta - 2\theta$  scans (Fig. 3(a)) for each-type of the  $VO_2$  film. Since morphological effects (Eq. (3)) are independent of  $h_z$ , whereas heterogeneous strain effects (Eq. (4)) scale with  $h_z$ , the analysis of several  $(0k0)$  reflections is required to distinguish between morphology-induced ( $\langle t \rangle$  and  $\sigma_t$ ) and strain-induced ( $\varepsilon_{zz}$ ) features. We used here the  $(020)_{VO_2}$  and  $(040)_{VO_2}$  reflections (for conciseness only the  $(020)_{VO_2}$  is shown Fig. 2). The simulation results show that the peak profiles were largely dominated by heterogeneous strain effects so that the roughness could not be accurately determined (as this requires clearly visible interference fringes). The roughness was hence fixed to its value deduced by AFM. Moreover, the tail index of the distribution function was in the 1.6-1.7 range for all samples indicating a significant non-Gaussian distribution of strain in the direction normal to the surface. The results inferred from the simulations are given in Table I. The film thickness is close to the 100 nm nominal value targeted during the film growth, with

a somewhat higher value for the as-grown sample. We should point out that the level of heterogeneous strain, as given by  $\varepsilon_{zz}$ , is approximately 4 times higher in the as-grown film than in the annealed and discharge films, which indeed indicates a higher defect density for this particular film, as suggested in the previous section.

### C. In-plane nanostructure

Let us now consider the  $\omega$ -scans, represented in Fig. 3(b) for each type of VO<sub>2</sub> layers. The as-grown film exhibits a broad peak shape, whereas the annealed sample exhibit a peculiar two-component profile shape, comprising a narrow (coherent) peak superimposed with a broad (diffuse) peak. This behavior is characteristic of thin films in which the random lattice distortions (rotations) are confined into regions of limited spatial extension, quantified by the correlation length  $\xi$ <sup>38,39</sup>. The coherent peak then originates from the long range crystalline order, whereas the broad diffuse peak originates from the highly distorted regions. Although such peak shapes are sometimes simulated with two different analytical functions, only a numerical simulation of such peaks allows one to determine the mosaicity  $\varepsilon_{xz}$ , the correlation length  $\xi$  as well as the lateral coherence length  $D$  (in-plane crystallite size) as long as the coherent peak is visible. The expression of the diffracted intensity in the direction parallel to the surface, for a symmetrical (0 $k$ 0) reflection with reciprocal lattice vector (0,  $h_z$ , 0) is given by<sup>36</sup>:

$$I(q_x) = \int dx.R(x)V(x)G(x)\exp(iq_x z) \quad (5)$$

where  $q_x$  is the deviation (in the  $x$  direction) of the scattering vector from the Bragg position. We show below that in the in-plane direction the crystallites building up the film are much larger than in the out-of-plane direction. Consequently, in the present case, the  $\omega$ -scans are much less sensitive to the crystallite size (and size fluctuation) than the  $\theta - 2\theta$  scans, so that an accurate determination of the in-plane crystallite size and shape is not conceivable. The choice of a particular crystallite shape and size distribution is therefore unimportant. In the following we shall consider crystallites having the shape of parallelepipeds (the dimensions of which are distributed according to a lognormal distribution) with average edge length  $\langle D \rangle$  and thickness  $\langle t \rangle$ , as detailed previously. The corresponding expression of  $V(x)$  can be found in<sup>36</sup>. The correlation function  $G(x)$  is similar to  $G(z)$  [34]:

$$G(x) = \exp\left(-\frac{1}{2}|h_x z|^\gamma \varepsilon_{xz}^\gamma\right) \quad (6)$$

The main difference with equation (4) is that  $G(x)$  involves the off-diagonal component of the heterogeneous strain tensor  $\varepsilon_{xz}$ , which corresponds to the characteristic width of the probability distribution function  $\delta e_{xz}$  ( $\delta e_{xz}$  being the angular deviation from the perfect (010)<sub>VO2</sub> || (001)<sub>Al2O3</sub> orientation).  $\varepsilon_{xz}$  hence simply corresponds to

the mosaicity. To account for the spatial confinement of the mosaicity it is necessary to introduce an additional parameter: the correlation length  $\xi$ . For length scales smaller than  $\xi$ , the rotations of the lattice planes are correlated giving rise to a mosaicity  $\varepsilon_{xz} = \varepsilon_0$ , whereas for length scales larger than  $\xi$ , the rotations of the lattice planes are uncorrelated so that the mosaicity asymptotically drops to 0. Such a behavior can be described with the following equation<sup>38</sup>:

$$\varepsilon_{xz}(x) = \frac{\varepsilon_0 \xi}{x} \left[1 - \exp\left(-\frac{x}{\xi}\right)\right] \quad (7)$$

Equations (4)-(6) have been used to simulate the experimental  $\omega$ -scans, Fig. 2(b). As in the case of the simulations of the  $\theta - 2\theta$  scans, the determination of the nanostructural parameters requires at least two (0 $k$ 0) reflection peaks. We here also use the (020)<sub>VO2</sub> and (040)<sub>VO2</sub> reflections (for conciseness only the (020)<sub>VO2</sub> is shown Fig. 2). The simulation results are given in Table I. The lateral crystallite size can be determined when the coherent peak is visible and is found to lie in the 300-400 nm range. Comparing the as-grown and the annealed films, it appears that in the annealed film, the mosaicity is confined into narrow regions ( $\xi = 9.5$  nm and a mosaicity of 0.68°), whereas for the as-grown film it appears that, while the mosaicity is only slightly larger (0.91°) it affects the whole film volume ( $\xi \gg t$ ) suggesting an altered crystalline quality, in good agreement with the higher level of heterogeneous strain obtained from the  $\theta - 2\theta$  scans.

## IV. DISCUSSION

### A. Nature of the defects

The confinement of the lattice distortions is in good agreement with the domain-matching growth mechanism for the annealed films, evidenced in<sup>35</sup>. Indeed, in this mechanism geometrical dislocations are directly generated at the interface during growth and do not require the glide of misfit dislocations from the surface to the interface. Since there are no threading segments associated with these dislocations the strain is confined close to the interface and high quality films can therefore be grown despite the lattice mismatch<sup>33,34</sup>. In the Supplementary Material we show that, in the case of stoichiometric films, containing solely geometrical dislocations, the correlation length  $\xi$  actually corresponds to the thickness of the distorted interfacial region.

The fact that the distortions affects the whole film volume in the as-grown sample ( $\xi \gg t$ ), instead of being confined at the interface, indicate that the state of strain in the film is dominated by defects of a different nature than geometrical dislocations; defects that are annihilated during O<sub>2</sub> annealing. Concomitantly, we also observe a decrease in the defect density (as shown by the reduction of the level heterogeneous strain from 0.41% to 0.11%) and a significant decrease in the lattice

parameter (from 4.5644 Å to 4.5101 Å). These observations are very well explained by the presence of oxygen vacancies in the as-grown films which are eliminated during the oxygen annealing. Oxygen vacancies are known to produce a swelling of the VO<sub>2</sub> unit-cell<sup>43</sup>. The swelling of the unit-cell can be explained both by the electrostatic repulsion between vanadium ions around the vacancies and the increase in ionic radius of the vanadium ions when reducing from V<sup>4+</sup> (0.63 Å) to V<sup>3+</sup> (0.74 Å), this reduction being imposed by charge neutrality, *i.e.*  $O^{2-} \rightarrow 1/2O_2(g) + V_O + 2e^-$  and  $2V^{4+} + 2e^- \rightarrow 2V^{3+}$ . Finally the distortion field around the vacancies<sup>37</sup> accounts for the higher level of heterogeneous strain  $\varepsilon_{zz}$  in the as-grown sample.

A further indication in this direction is given by the discharge film. In this process the RF plasma discharge enhances the oxygen decomposition (and therefore the ion reactivity in the gas phase) as well as the mobility of the deposited atoms at the substrate surface, and the films should hence exhibit a stoichiometry close to the nominal value. This is confirmed by the fact that the discharge film exhibits a confined mosaicity and a level of heterogeneous strain comparable to the annealed films. However, the fact that the lattice parameter in the discharge film is larger than expected suggests that the discharge process is less efficient than thermal annealing in ensuring the correct stoichiometry, and this film might still contain oxygen vacancies responsible for the swelling of the unit-cell.

## B. Electrical properties

Fig. 4 shows the evolution of the electrical resistivity  $\rho(T)$  during a heating/cooling cycle (temperature ramped up and down between 25 and 95°C) for all type of VO<sub>2</sub> films. The variation of the resistivity with temperature is typical of first-order transitions as observed in VO<sub>2</sub> bulk and thin films materials: a drastic decrease of the resistivity by more than four orders of magnitude as the temperature is ramped up and reaches the transition temperature associated with the metal-insulator transition ( $T_{MIT}^{up}$ )<sup>1,2</sup>. The resistivity varies between 7.7 Ω.cm at 25°C and  $2.7 \times 10^{-4}$  Ω.cm when the film is heated to 95°C (resistivity ratio of  $2.85 \times 10^4$ ). The resistivity ratio is often used as a measure of the film quality, with the highest value of  $9 \times 10^4$  being observed in the best single crystals<sup>14</sup>. The films grown in the present study are hence close to the best reported to date and exhibit a similar (though somewhat higher) ratio than previously reported VO<sub>2</sub> films grown by electron-beam evaporation on sapphire substrates<sup>15,16</sup>.

During the cooling process, the resistivity recovers its initial low-temperature value. In the following we define the transition temperatures for each of the resistivity hysteresis branches ( $T_{MIT}^{up}$  for heating and  $T_{MIT}^{down}$  for cooling) as the temperatures where the first-order derivatives ( $d \log 10\rho/dT$ ) of the corresponding  $\rho(T)$  curves reach their maximum. We obtain  $T_{MIT}^{up} = 76^\circ\text{C}$

and a  $T_{MIT}^{down} = 72.2^\circ\text{C}$ , corresponding to an average  $T_{MIT} = 74.1^\circ\text{C}$  (the hysteresis width is 3.8°C and the transition extends over  $\sim 10^\circ\text{C}$ ). It can be readily noticed that this value is higher than the theoretical transition temperature (68°C). We have previously shown<sup>35</sup> that this offset from the theoretical value can be explained by the tensile strain exerted on the V-V chains, in good agreement with many experimental and theoretical studies<sup>19–26</sup>.

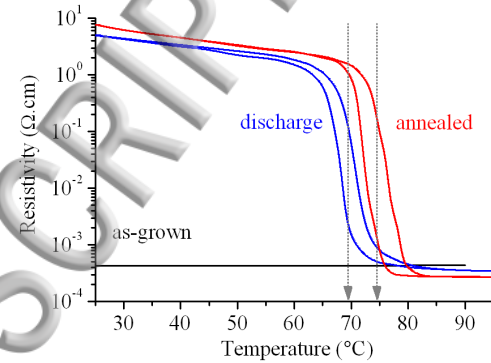


FIG. 4. Evolution of the electrical resistivity with temperature for each type of film. Black line: as-grown; red line: annealed; blue line: discharge. The arrows indicate the transition temperature.

The discharge-type 100-nm thick film exhibit a similar resistivity hysteresis shape as the annealed sample, but with an average MIT transition temperature shifted to 69.5°C and a resistivity ratio reduced to  $1.44 \times 10^4$ . It shows both a lower resistivity, of 5 Ω.cm, in the insulating phase at 25°C and a slightly degraded metallic state with a resistivity of  $3.4 \times 10^{-4}$  Ω.cm at 95°C.

These observations are in good agreement with the presence of oxygen vacancies in the film which are known to shift the transition towards lower temperatures and reduce the resistivity ratio<sup>27–29</sup>. In short, the presence of oxygen vacancies reduces the hybridization between the V3d and O2p orbitals which results in reduction of the band gap, and the extra electrons introduce donor levels in the band gap<sup>27,28,30</sup>. In the low temperature region of the electrical hysteresis cycles (25–55°C), the conductivity obeys an Arrhenius-type law, in the form of  $\sigma = \sigma_0 \exp(-E_A/kT)$  where  $\sigma$  is the conductivity,  $\sigma_0$  is the conductivity at  $T = 0K$ ,  $E_A$  is the activation energy,  $k$  is Boltzmann's constant and  $T$  is the temperature. The values of the activation  $E_A$  extracted from the curves shown in Fig. 4, are of 0.273 eV for the annealed VO<sub>2</sub> films and 0.236 eV for the discharge-type layers. A value of 0.3 eV is expected for the monoclinic (insulating) phase of VO<sub>2</sub> since the value of the activation energy should be equal to the half of the optical bandgap (0.6 eV)<sup>44</sup>, considering that the Fermi level is situated in the middle of the gap of the VO<sub>2</sub>, as is the case for an intrinsic semi-conductor. Such values are for instance reported in high-quality single-domain VO<sub>2</sub> nanobeams<sup>45</sup>. Values

as low as 0.13-0.16 eV are often reported for thin VO<sub>2</sub> films with lattice defects<sup>46,47</sup>. Thus, the activation energies values for both type of samples, close to theoretical values, confirm their high quality in terms of electrical and structural properties. The lower value of  $E_A$  for the discharge samples suggest (besides the presence of interface structural defects as revealed for both samples by the XRD analysis) the onset of additional donor levels which may contract the bandgap, in good agreement with the presence of oxygen vacancies<sup>29</sup>. Regarding the as-grown VO<sub>2</sub> sample, it exhibit a purely metallic behavior (Fig. 4), with the MIT being suppressed from the temperature range investigated, which indicates a large concentration of oxygen vacancies stabilizing the metallic phase<sup>29</sup>.

### C. Vibrational properties

The metallic nature of the as-grown-type VO<sub>2</sub> film was confirmed also by Raman spectroscopy measurements. Fig. 5 displays the Raman spectra of the sapphire substrate, the as-grown, discharge and annealed VO<sub>2</sub> films. While the as-grown film shows a metallic-like behavior with no spectral features (akin to the VO<sub>2</sub> R phase), the annealed and discharge VO<sub>2</sub> samples exhibit Raman spectra indicative of a high quality monoclinic M1 VO<sub>2</sub> phase with  $P2_1/c$  symmetry<sup>48-50</sup> which are consistent with previous reports on VO<sub>2</sub> micro-crystalline thin films and single-crystal microbeams<sup>51-53</sup>. The M1 phase is identified by the  $\omega_{v1}$  and  $\omega_{v2}$  modes at 195 cm<sup>-1</sup> and 225 cm<sup>-1</sup>, respectively, associated with the V-V lattice motion while the rest of the peaks (including the dominant broad  $\omega_0$  phonon frequency which peaks at ~616 cm<sup>-1</sup>) are assigned to V-O vibrational modes<sup>48,51,53</sup>.

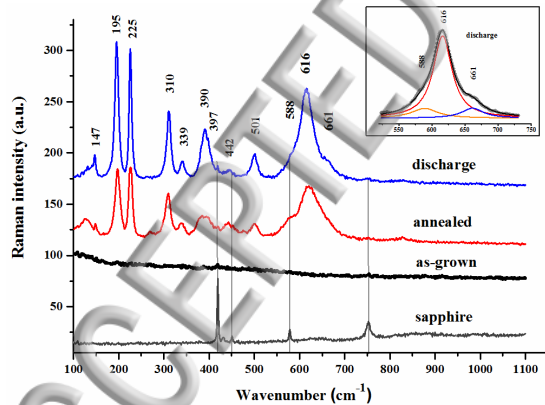


FIG. 5. Raman spectra of the sapphire substrate, as-grown, discharge and annealed VO<sub>2</sub> films. Inset: fit of the 616 cm<sup>-1</sup> line with 3 individual lines located at 588, 616 and 661 cm<sup>-1</sup>.

The Raman signature of the sapphire substrate is weak, but non zero, in the VO<sub>2</sub> films, indicating that the entire film's volume was probed by the incident radiation. The presence of the 147 cm<sup>-1</sup> peak was assigned to a Raman Ag symmetry mode<sup>48-50</sup> associated with soft phonons while the broad peak at 616 cm<sup>-1</sup> is a superposition of the 616 cm<sup>-1</sup> peak with Ag sym-

metry, the 661 cm<sup>-1</sup> and 588 cm<sup>-1</sup> Raman peaks with Bg symmetry (although the last one was often assigned to the Ag mode)<sup>50,54</sup> (inset in Fig. 5). The presence of the low frequency features below 147 cm<sup>-1</sup> for both 100-nm thick annealed and discharge VO<sub>2</sub> - sapphire interface (rigid layer modes defined as external vibration/translation modes of the structural lattice units) associated with different levels of strain and geometrical dislocations at the interface (as also indicated by the XRD analysis) or even indicative of the presence of small amounts of other vanadium oxide phases (V<sub>2</sub>O<sub>5</sub>, V<sub>6</sub>O<sub>13</sub>)<sup>55</sup>. The broadening of the low frequency peak below 140 cm<sup>-1</sup> (suggesting the addition of multiple layer modes) in the case of the annealed VO<sub>2</sub> film can be correlated with the higher mosaicity observed in this sample (0.68° instead of 0.28°) bearing in mind that for both samples, the mosaicity is confined in narrow regions at the interface.

### V. CONCLUSIONS

High-quality, large area epitaxial VO<sub>2</sub> films grown on (001)-sapphire substrate have been grown by electron evaporation. Whereas as-grown film exhibit a poor structural quality (large deviation from stoichiometry, large mosaicity and large strains) and a purely metallic behavior, films annealed in oxygen atmosphere exhibit an excellent electrical behavior, with a resistivity ratio across the MIT of more than four orders of magnitude. Consistently, these films also exhibit excellent structural properties with a low level of heterogenous strain, a mosaicity confined into narrow regions close to the interface and a level of strain solely due to the film/substrate thermal expansion mismatch, in good agreement with the domain-matching growth mechanism expected in this system. Alternatively, we showed that it is possible to obtain high quality films with an RF discharge during deposition, and which do not require the additional annealing step. Such films exhibit similar electrical properties and only slightly degraded structural properties. In particular, we observed an oxygen deficiency in such films which (i) yield a swelling of the unit-cell and (ii) a shift of the MIT towards lower temperatures.

### SUPPLEMENTARY MATERIAL

See supplementary material for the interpretation of the phenomenological parameters (used in the present model) in terms of dislocation characteristics.

### ACKNOWLEDGMENTS

VT is grateful to région Limousin (France) and Labex SigmaLim for financial support.

<sup>1</sup>F. Morin, Phys. Rev. Lett. **3**, 34 (1959).

- <sup>1</sup>N. F. Mott, *Metal-Insulator Transitions*, edited by T. F. N. York (Taylor & Francis : New York, 1974).
- <sup>2</sup>C. Galleri, C. Tóth, C. W. Siders, J. A. Squier, F. Ráksi, P. Forget, and J. C. Kieffer, *Phys. Rev. Lett.* **87**, 237401 (2001).
- <sup>4</sup>H.-T. Kim, B.-G. Chae, D.-H. Youn, S.-L. Maeng, G. Kim, K.-Y. Kang, and Y.-S. Lim, *New J. Phys.* **6**, 52 (2004).
- <sup>5</sup>J. Leroy, A. Bessaudou, F. Cosset, and A. Crunteanu, *Thin Solid Films* **520**, 4823 (2012).
- <sup>6</sup>A. Crunteanu, J. Givernaud, J. Leroy, D. Mardivirin, C. Champeaux, J.-C. Orlianges, A. Cathérinot, and P. Blondy, *Sci. Tech. Adv. Mater.* **11**, 065002 (2010).
- <sup>7</sup>A. Beaumont, J. Leroy, J.-C. Orlianges, and A. Crunteanu, *J. Appl. Phys.* **115**, 154502 (2014).
- <sup>8</sup>A. Crunteanu, M. Fabert, J. Cornette, M. Colas, J.-C. Orlianges, A. Bessaudou, and F. Cosset, *Proc. SPIE* **9364**, 93640 (2015).
- <sup>9</sup>J. Nag and R. F. H. Jr, *J. Phys.: Condens. Matter* **20**, 264016 (2008).
- <sup>10</sup>D. Ruzmetov, S. D. Senanayake, V. Narayanamurti, and S. Ramanathan, *Phys. Rev. B* **77**, 195442 (2008).
- <sup>11</sup>Y. Nihei, Y. Sasakawa, and K. Okimura, *Thin Solid Films* **516**, 3572 (2008).
- <sup>12</sup>T. D. Manning and I. P. Parkin, *J. Mater. Chem.* **14**, 2554 (2004).
- <sup>13</sup>L. L. Fan, S. Chen, Y. F. Wu, F. H. Chen, W. S. Chu, X. Chen, C. W. Zou, and Z. Y. Wu, *Appl. Phys. Lett.* **103**, 131914 (2013).
- <sup>14</sup>H. Zhang, L. Zhang, D. Mukherjee, Y.-X. Zheng, R. C. Haismaier, N. Alem, and R. Engel-Herbert, *Nat. Comm.* **6**, 8475 (2015).
- <sup>15</sup>F. C. Case, *J. Vac. Sci. Technol. A* **5**, 1762 (1987).
- <sup>16</sup>J. F. D. Natale, P. J. Hood, and A. B. Harker, *J. Appl. Phys.* **66**, 5844 (1989).
- <sup>17</sup>R. G. Mani and S. Ramanathan, *Appl. Phys. Lett.* **91**, 062104 (2007).
- <sup>18</sup>R. E. Marvel, K. Appavoo, B. K. Choi, J. Nag, and R. F. Haglund, *Appl. Phys. A* **111**, 975 (2013).
- <sup>19</sup>R. Molaie, R. Bayati, F. Wu, and J. Narayan, *J. Appl. Phys.* **115**, 164311 (2014).
- <sup>20</sup>N. Aetukuri, A. Gray, M. Drouard, M. Cossale, L. Gao, A. Reid, R. Kukreja, H. Ohlag, C. Jenkins, E. Arenholz, K. Roche, H. Dürr, M. Samant, and S. Parkin, *Nature Phys.* **10**, 1038 (2013).
- <sup>21</sup>E. Abreu, M. Liu, J. Lu, K. G. West, S. Kittiwatanakul, W. Yin, S. A. Wolf, and R. D. Averitt, *New J. Phys.* **14**, 083026 (2012).
- <sup>22</sup>Y. Muraoka and Z. Hiroi, *Appl. Phys. Lett.* **80**, 583 (2002).
- <sup>23</sup>H. Paik, J. A. Moyer, T. Spila, J. W. Tashman, J. A. Mundy, E. Freeman, N. Shukla, J. M. Lapano, R. Engel-Herbert, W. Zander, J. Schubert, D. A. Muller, S. Datta, P. Schiffer, and D. G. Schlom, *Appl. Phys. Lett.* **107**, 163101 (2015).
- <sup>24</sup>L. Fan, S. Chan, Z. Luo, Q. Liu, Y. Wu, L. Song, D. Ji, P. Wang, W. Chu, C. Gao, C. Zou, and Z. Wu, *Nano Lett.* **14**, 4036 (2014).
- <sup>25</sup>C. Chen, Y. Zhu, Y. Zhao, J. Lee, H. Wang, A. Bernussi, M. Holtz, and Z. Fan, *Appl. Phys. Lett.* **97**, 211905 (2010).
- <sup>26</sup>K. Okimura and J. Sakai, *Jpn. J. Appl. Phys.* **48**, 045504 (2009).
- <sup>27</sup>L. Fan, Y. Wu, C. Si, G. Pan, C. Zou, and Z. Wu, *Appl. Phys. Lett.* **102**, 011604 (2013).
- <sup>28</sup>P. Zhang, K. Jiang, Q. Deng, Q. You, J. Zhang, J. Wu, Z. Hu, and J. Chu, *J. Mater. Chem. C* **3**, 5033 (2015).
- <sup>29</sup>J. Jeong, N. Aetukuri, T. Graf, T. D. Schladt, M. G. Samant, and S. S. P. Parkin, *Science* **339**, 1402 (2013).
- <sup>30</sup>L. Chen, Y. Cui, S. Shi, B. Liu, H. Luo, and Y. Gao, *RSC Adv.* **6**, 86872 (2016).
- <sup>31</sup>F. Wong, Y. Zhou, and S. Ramanathan, *J. Cryst. Growth* **364**, 74 (2013).
- <sup>32</sup>D. Kucharczyk and T. Niklewski, *J. Appl. Crystallogr.* **12**, 370 (1979).
- <sup>33</sup>A. Trampert and K. Ploog, *Cryst. Res. Technol.* **35**, 793 (2000).
- <sup>34</sup>J. Narayan and B. C. Larson, *J. Appl. Phys.* **93**, 278 (2003).
- <sup>35</sup>V. Théry, A. Boule, A. Crunteanu, J. C. Orlianges, A. Beaumont, R. Mayet, A. Mennai, F. Cosset, A. Bessaudou, and M. Fabert, *Phys. Rev. B* **93**, 184106 (2016).
- <sup>36</sup>A. Boule, F. Conchon, and R. Guinebrière, *Acta Crystallogr. Sect. A* **62**, 11 (2006).
- <sup>37</sup>U. Pietsch, V. Holy, and T. Baumbach, *High-resolution X-ray scattering - From thin films to lateral nanostructures*, edited by Springer (Springer, 2004).
- <sup>38</sup>A. Boule, R. Guinebrière, and A. Dauger, *J. Phys. D: Appl. Phys.* **38**, 3907 (2005).
- <sup>39</sup>A. Boule, R. Guinebrière, and A. Dauger, *J. Appl. Phys.* **97**, 073503 (2005).
- <sup>40</sup>F. Conchon, A. Boule, R. Guinebrière, E. Dooryhée, J.-L. Hodeau, C. Girardot, S. Pignard, J. Kreisel, and F. Weiss, *J. Phys.: Condens. Matter* **20**, 145216 (2008).
- <sup>41</sup>A. Boule and A. Debelle, *Phys. Rev. Lett.* **116**, 245501 (2016).
- <sup>42</sup>A. Boule, I. C. Infante, and N. Lemée, *J. Appl. Crystallogr.* **49**, 845 (2016).
- <sup>43</sup>C. H. Griffiths and H. K. Eastwood, *J. Appl. Phys.* **45**, 2201 (1974).
- <sup>44</sup>C. N. Berglund and H. J. Guggenheim, *Phys. Rev.* **185**, 1022 (1969).
- <sup>45</sup>J. Wei, Z. Wang, W. Chen, and D. H. Cobden, *Nat Nano* **4**, 420 (2009).
- <sup>46</sup>F. Guinneton, L. Sauques, J. Valmalette, F. Cros, and J. Gavarrri, *J. Phys. Chem. Solids* **62**, 1229 (2001).
- <sup>47</sup>J.-C. Orlianges, J. Leroy, A. Crunteanu, R. Mayet, P. Carles, and C. Champeaux, *Appl. Phys. Lett.* **101**, 133102 (2012).
- <sup>48</sup>M. Zaghrioui, J. Sakai, N. H. Azhan, K. Su, and K. Okimura, *Vibr. Spectrosc.* **80**, 79 (2015).
- <sup>49</sup>I. N. Goncharuk, A. V. Ilinskiy, O. E. Kvashenkina, and E. B. Shadrin, *Phys. Solid State* **55**, 164 (2013).
- <sup>50</sup>P. Schilbe and D. Maurer, *Mat. Sci. Eng. : A* **370**, 449 (2004).
- <sup>51</sup>J. I. Sohn, H. J. Joo, K. S. Kim, H. W. Yang, A.-R. Jang, D. Ahn, H. H. Lee, S. Cha, D. J. Kang, J. M. Kim, and M. E. Welland, *Nanotechnology* **23**, 205707 (2012).
- <sup>52</sup>K. Okimura, N. Hanis Azhan, T. Hajiri, M. Kimura, S. and Zaghrioui, and J. Sakai, *J. Appl. Phys.* **115**, 153501 (2014).
- <sup>53</sup>J. M. Atkin, S. Berweger, E. K. Chavez, M. B. Raschke, J. Cao, W. Fan, and J. Wu, *Phys. Rev. B* **85**, 020101 (2012).
- <sup>54</sup>X.-B. Chen, *J. Korean Phys. Soc.* **58**, 100 (2011).
- <sup>55</sup>C. Julien, G. A. Nazri, and O. Bergström, *Phys. Status Solidi (b)* **201**, 319 (1997).

